Dalton Transactions

ROYAL SOCIETY OF CHEMISTRY

PAPER

Published on 24 February 2026

Cite this: *Dalton Trans.*, 2026, **55**, 4584

Partially substituted magnetic ferrites as Pt-free catalysts for hydrogen evolution from water photo-electrolysis

Luana De Pasquale,†[a] Tatiana Rodriguez-Flores,†[b] Daniele Valenzisi,[b] Falak Shafiq,[b] Roberto Scotti,[b] Francesco Tavella,[a] Matteo Cantoni,[c] Maria Vittoria Dozzi,[d] Chiara Genovese *[a] and Roberto Nisticò *[b]

The global energy landscape, still heavily dependent on fossil fuels, has intensified the search for sustainable alternatives. Specifically, the interest is focused on a clean energy source such as hydrogen, through the development of cost-effective and efficient photo-electrocatalysts based on earth-abundant elements. In this context, magnetic spinel ferrites have attracted attention as low-cost, Pt-free catalysts for the photo-electrocatalytic hydrogen evolution reaction (HER). In this work, a series of spinel ferrites, $CuFe_2O_4$, $CoFe_2O_4$, $ZnFe_2O_4$, and partially substituted $CuFe_2O_4$ with Co^{2+} or Zn^{2+} (Cu*X*Co*Y*Fe or Cu*X*Zn*Y*Fe, where *X* is the % of Cu, and *Y* is the % of substituting cation) were synthesized *via* a soft-chemistry co-precipitation route and systematically evaluated as photo-electrocatalysts for HER in neutral media. Structural and morphological analyses confirmed the formation of single-phase spinel with tunable lattice parameters and crystallite sizes. SEM revealed a progressive morphology transition from anisotropic structures to compact particles in Co- and Zn-substituted systems, while magnetic characterization evidenced superparamagnetic behavior in all samples, with Co substitution enhancing the saturation magnetization and Zn substitution modulating the saturation magnetization depending on the concentration. Electrochemical and photo-electrochemical testing demonstrated that controlled Co^{2+} and Zn^{2+} doping significantly improved charge transfer, HER activity, and selectivity. Notably, in photo-electrocatalytic experiments, Cu95Zn5Fe achieved the highest hydrogen production (304.3 mmol g^{-1}) with a Faradaic Efficiency of 94%, while Cu75Co25Fe reached nearly 100% efficiency in the same conditions. Electrochemical impedance spectroscopy further confirmed reduced interfacial resistance and improved charge transport in the substituted ferrites. These findings highlight the potential of tailored magnetic spinel ferrites for efficient, sustainable hydrogen generation and provide design guidelines for optimizing photo-electrocatalytic performance by controlling Co^{2+} and Zn^{2+} content into $CuFe_2O_4$.

Received 17th December 2025,
Accepted 23rd February 2026

DOI: 10.1039/d5dt03018h

rsc.li/dalton

Introduction

The relentless consumption of carbon-based fossil fuels has intensified the global energy crisis and exacerbated environmental challenges, including climate change and pollution.[1] Hydrogen as a carbon-free energy source is widely recognized as a cornerstone for a sustainable energy transition, offering a clean, high-density energy alternative capable of addressing both the energy crisis and environmental issues.[2,3] Among various approaches to hydrogen production, both electrochemical and photo-electrochemical water splitting stand out as ones of the most promising methods to obtain high purity hydrogen without carbon footprints through hydrogen evolution reaction (HER).[4] HER produces molecular hydrogen from water through different pathways depending on the pH of the system, typically proceeding *via* either Volmer–Heyrovsky or the Volmer–Tafel mechanism. In both routes, hydrogen adsorption on the catalyst surface leads to the formation of adsorbed intermediates (H_{ad}). However, excessively weak or strong hydrogen surface interactions can hinder the overall kinetics by limiting either hydrogen adsorption or molecular desorption.[5] Therefore, an efficient HER photo-

[a]*University of Messina, Department of Chemical, Biological, Pharmaceutical and Environmental Sciences (ChiBioFaram), Viale F.S. D'Alcontres 31, 98166 Messina, Italy. E-mail: chiara.genovese@unime.it*
[b]*University of Milano-Bicocca, Department of Materials Science, U5, INSTM, Via R. Cozzi 55, 20125 Milano, Italy. E-mail: roberto.nistico@unimib.it*
[c]*Politecnico di Milano, Department of Physics, Via G. Colombo 81, 20133 Milano, Italy*
[d]*Università degli studi di Milano, Dipartimento di Chimica, Via C. Golgi 19, 20133 Milano, Italy*
† Both authors contributed equally to this work.

catalyst should exhibit a hydrogen adsorption free energy (ΔG_H) close to zero, ensuring optimal adsorption–desorption balance.[6]

Nevertheless, the development of low-cost, earth-abundant, stable and efficient electro- and photocatalysts with low overpotentials for HER, capable of replacing noble metal such as Pt while maintaining high efficiency and cost-effectiveness, remains a great challenge.[2,7]

Among the various alternative materials investigated, transition metal oxides with the general formula AB_2O_4 (where A and B denote divalent and trivalent cations, respectively) have attracted significant attention for a wide range of applications, particularly in photo-electrochemical processes.[2] Their unique crystalline structure enables a flexible distribution of cationic oxidation states, allowing A and B ions to easily switch between the bivalent and trivalent oxidation states. This redox adaptability, combined with their magnetic properties, makes these oxides especially valuable in photo-electrochemical processes, where the catalyst must undergo either reduction or oxidation prior to the transformation of the substrate.[8] Among this family, spinel ferrites, which are multicomponent metal oxides with the general formula MFe_2O_4 (M = Cu, Co, Zn, *etc.*), stand out. In fact, their cation arrangement enables precise tuning of electronic, optical and catalytic properties through controlled cation substitution.[9,10]

In the field of electrocatalysis, spinel ferrites have been extensively studied as efficient catalysts for HER in both acidic and neutral media.[11] Their intrinsic electronic structure facilitates optimized adsorption–desorption kinetics of hydrogen intermediates, following the Volmer–Heyrovsky–Tafel mechanism.[12,13] For instance, spinel $CuFe_2O_4$ is a p-type semiconductor that can crystallize in either cubic or tetragonal phases, depending on the cation distributions at the A and B sites. $CuFe_2O_4$ is widely used in HER due to its low band gap energy (*ca.* 1.4 eV) and negatively positioned conduction band.[14] In this context, Danish *et al.*[15] reported that $CuFe_2O_4$ exhibits superior HER performance in alkaline media compared to Cu_2O and Fe_2O_3 attributed to improved charge transfer and high specific capacitance (978 F g^{-1}) and energy density (66 W h kg^{-1}). The material showed an onset potential of 0.09 V, a low over potential of 69 mV at a current density of 10 mA cm^{-2}, and a Tafel slope of 47.2 mV dec^{-1}, making it suitable for energy conversion applications. Similarly, $CoFe_2O_4$ displays good electrical conductivity and charge mobility due to the Co–O–Fe network. For instance, Nivetha and co-workers[16] synthesized $CoFe_2O_4$- and $NiFe_2O_4$-based graphene nanocomposites for electrochemical HER and observed that graphene modification reduced the onset potential and improved the current density, indicating enhanced electrocatalytic activity toward HER in acidic media, where $CoFe_2O_4$–graphene nanocomposite displayed the best performance with lower charge transfer resistance compared to $NiFe_2O_4$–graphene. Conversely, $ZnFe_2O_4$, a non-magnetic ferrite with a wide band gap, generally shows weak electrocatalytic activity, but better stability, often serving as a structural modulator in mixed ferrite systems.[17,18] In a related study, Nivetha and Grace[19] evaluated the HER activity of $ZnFe_2O_4$-based graphene nanocomposites and observed an improvement in the electrochemical performance compared to the pure ferrite, achieving a current density of 47 mA cm^{-2} and a Tafel slope a 114.3 mV dec^{-1}, following a Volmer mechanism during HER in acidic medium.

Moving beyond pure electrocatalysis, photo-electrocatalysis (PEC) introduces an additional level of complexity and efficiency by exploiting photon energy to facilitate charge generation and reduce the overpotential required for HER.[20,21] Spinel ferrites are considered excellent candidates for PEC water splitting owing to their suitable band-edge positions for proton reduction (ECB < 0 V *vs.* RHE) as well as their visible-light absorption capability.[22,23] In this regard, Tran *et al.*[24] investigated the photo-electrochemical performance of $CuFe_2O_4$/TCPP (*i.e.*, tetrakis(4-carboxyphenyl) porphyrin) nanocomposites for HER, demonstrating an enhancement in PEC activity due to the efficient charge separation and exciton-coupled charge transfer between $CuFe_2O_4$ nanoparticles and TCPP nanofibers, highlighting its potential as a promising photoanode material for sustainable hydrogen generation. On the other hand, Salman *et al.*[25] synthesized PVP-coated and uncoated $Zn_xFe_2O_{4\pm\delta}$ (x = 0.98–1.02) nanostructures *via* a one-step hydrothermal method. Among these, the 2% Zn-deficient photoanode showed superior photo-electrochemical performance and higher photo-to-hydrogen conversion efficiency, attributed to defect-induced oxygen vacancies that improved charge separation and interfacial charge transfer.

Furthermore, as reported by Amin *et al.*[26] in a study dedicated on the design of PECs for CO_2RR, the introduction of doping elements in ferrites' lattice structure, if properly done, is able to tailor both electronic and surface properties that might enhance ferrites' light absorption ability, charge separation, and redox activity. However, even if $CuFe_2O_4$ is well-known for being a good photocathodic materials,[27] only few studies explored how doping with different elements affects not only the structural, and magnetic properties of $CuFe_2O_4$, but also influences the PEC performance of these systems in water electrolysis.

Hence, in the present study, a systematic investigation of $CuFe_2O_4$, $CoFe_2O_4$, and $ZnFe_2O_4$ spinel ferrites, as well as $CuFe_2O_4$ partially substituted with Co^{2+} and Zn^{2+}, was conducted to elucidate the structure–property–activity relationships and the role of doping governing their photo-electrocatalytic performance toward HER in neutral media by performing a comparative evaluation of the different dopants' effect. Materials were synthesized *via* a controlled co-precipitation route, and comprehensively characterized through structural, morphological, magnetic, and photo-electrochemical analyses. All samples were evaluated under identical photo-electrochemical testing conditions. Moreover, the main aim of the present work is to unravel how cationic substitution within the spinel lattice impacts charge-transfer resistance, photocurrent response, and overall hydrogen productivity, offering new insights into the rational design of magnetic ferrite-based photo-electrocatalysts for sustainable hydrogen production.

Experimental

Chemicals

Reactants: iron(III) nitrate nonahydrate ($Fe(NO_3)_3{\cdot}9H_2O$, 98.0–101.0% CAS 7782-61-8, Thermo Scientific), copper(II) nitrate trihydrate ($Cu(NO_3)_2{\cdot}3H_2O$, 99%, CAS 10031-43-3, Thermo Scientific), cobalt(II) nitrate hexahydrate ($Co(NO_3)_2{\cdot}6H_2O$, 99%, CAS 10026-22-9, Sigma-Aldrich), zinc(II) nitrate hexahydrate ($Zn(NO_3)_2{\cdot}6H_2O$, 98%, CAS 10196-18-6, Alfa Aesar), and sodium hydroxide pellets (NaOH, ACS reagent, ≥98%, CAS 1310-73-2, Sigma-Aldrich). Solutions and solvents: deionized water and acetone (CH_3COCH_3, CAS 67-64-1, Sigma-Aldrich) were used during washing procedures. Milli-Q water with a resistivity of 18.2 MΩ cm was used. All chemicals were used without further purification.

Synthesis of magnetic ferrite systems

The synthesis of the magnetic ferrite systems was prepared employing a co-precipitation method following a modified procedure from the literature.[28] In a typical synthesis, an aqueous solution containing both the iron(III) nitrate (3.3 g; 8.2 mmol) and the other metal precursor(s) (4.1 mmol, this way it was maintained the stoichiometric molar ratio Fe : M 2 : 1) was prepared in 75 mL of deionized water and stirred at room temperature (RT). Next, while maintaining the precursors solution under constant stirring, 5 M NaOH solution (15 mL) was added dropwise (delivery time: 10 minutes) to ensure the homogeneous precipitation of the metal cations (total vol. 90 mL). Afterward, the temperature of the solution was gradually increased from RT to 90 °C and maintained in isothermal conditions for two hours under continuous stirring. Subsequently, once the precipitation was completed, the solution was transferred into a Falcon tube for centrifugation (6000 rpm, 10 minutes) and washed 3 times with deionized water and once with acetone. The final precipitate was oven dried under air atmosphere at 80 °C overnight. The dried solid was gently crumbled inside an agate mortar, and thermally treated in a Carbolite CWF1200 muffle furnace (Carbolite, Hope, UK) with the following thermal program: (i) heating ramp from RT to 700 °C (heating rate: 10 °C min^{-1}), (ii) isothermal step at 700 °C for 5 h, and (iii) cooling step from 700 °C to 50 °C (cooling rate: 5 °C min^{-1}).[29] Once the reaction was completed, the calcined powders were removed from the furnace, cooled naturally to RT, further gently crumbled inside an agate mortar, and samples storage inside a closed glass vial. The obtained samples are defined as Cu100Fe (bare Cu ferrite, $CuFe_2O_4$), Co100Fe (bare Co ferrite, $CoFe_2O_4$), and Zn100Fe (bare Zn ferrite, $ZnFe_2O_4$). Fig. 1 shows a schematic representation of co-precipitation method employed to obtain the magnetic ferrite systems.

Moreover, by selecting Cu ferrite system as reference system, further magnetic ferrite samples were produced by partially replacing the nominal amount of Cu(II) with either Co(II) or Zn(II) ones, thus in order to maintain constant the stoichiometric molar ratio between divalent (*i.e.*, Cu(II), Co(II), Zn(II)) and trivalent (*i.e.*, Fe(III)) cations.

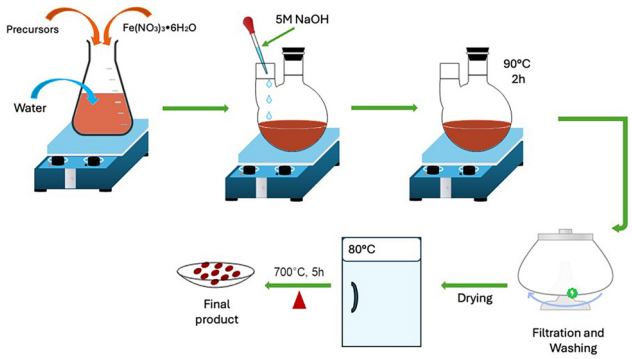

Fig. 1 Schematic representation of co-precipitation method employed for the synthesis of the magnetic ferrite systems.

The obtained samples are defined as either Cu*X*Co*Y*Fe or Cu*X*Zn*Y*Fe, where *X* is the % of Cu, and *Y* is the % of substituting elements (*e.g.*, Cu95Co5Fe is the 5% Co-substituted Cu ferrite, $Cu_{0.95}Co_{0.05}Fe_2O_4$). Table S1 (SI) reports the list of synthesized samples and their compositional parameters.

Characterization

X-ray powder diffraction (XRPD) patterns were recorded using a Rigaku Miniflex 600 diffractometer with a Cu source (40 kV, 15 mA). Data acquisition was performed over a 2θ range of 20–80°, with a step size of 0.02° and an angular velocity of 1.0° per minute. The PDXL-2 software was utilized to compare the obtained patterns with reference diffraction data from the ICDD database. The lattice parameters were also calculated using the PDXL-2 software. The crystallite average size was estimated using the Scherrer equation to the most intense diffraction peak of each ferrite:

$$\tau = \frac{k\lambda}{\beta(\cos\theta)} \quad (1)$$

where: τ is the average crystallite size (in nm), K is the shape factor (typically 0.9), λ is the X-ray wavelength (0.154 nm for a Cu source), β is the full width at half maximum (FWHM) of the selected Bragg peak after subtracting instrumental broadening (in radians), and θ is the Bragg angle (in radians). For the magnetic ferrite crystal phase, the selected Bragg angle refers to the (400) and (024) planes reflections at 43.2 ± 0.3° 2θ.

Scanning electron microscopy (SEM) micrographs were obtained using a Zeiss Gemini 500 microscope equipped with a field emission source (FEG) and a Bruker Quantax detector for energy-dispersive X-ray spectroscopy (EDS) microanalysis. The microscope was operating at an acceleration voltage of 5.00 kV. Micrographs were captured using the "in-lens" detector. Samples were deposited onto SEM stubs using a double-adhesive carbon tape, then they were covered with Au coating to prevent charging effects using a VPI SD-900C sputter coater.

The magnetic characterization was performed by Vibrating Sample Magnetometry (VSM), using an EZ-9 MicroSense Magnetometer, with resolution of 1 μemu and maximum field

of 2.25 T. The measurements were performed at RT, with the material contained in quartz cuvettes. The absence of any ferromagnetic spurious contribution from the cuvettes was verified before any measurement, and the diamagnetic contribution, intrinsic to the quartz material, measured on empty cuvettes was automatically subtracted.

Photo-electrochemical characterization and testing

The photo-electrochemical characterization (cyclic voltammetry – CV, chronoamperometry – CA, and electrochemical impedance spectroscopy – EIS) and the photo-electrocatalytic tests of H_2 production from water splitting of the ferrite-based samples (listed in Table S1, SI) were performed in the custom-made cell schematized in Fig. 2.

The three-electrode cell made of Plexiglass consists in two separate compartments, anodic and cathodic, divided by a Teflon reinforced Nafion membrane (N 324, supplied by *Ion Power*). A platinum electrode and an Ag/AgCl electrode (3 M KCl), supplied by *Amel*, served as the counter and reference electrodes, respectively, while the ferrite-based photocathode, acted as the working electrode. The ferrite-based photocathodes were prepared by drop-casting a solution containing the ferrite on a fluorine-doped tin oxide (FTO)-coated conductive glass (active area 1 cm^2). Specifically, the ferrite powder was first milled, then sonicated in isopropanol for 30 minutes. After that, it was deposited on the FTO-glass on a hot plate and dried at 120 °C overnight (loading 1 mg cm^{-2}). Other details of the electrode preparation were reported in SI.

All electrochemical measurements and photo-electrocatalytic tests were performed using a potentiostat/galvanostat (Autolab PGSTAT 204), in 0.1 M Na_2SO_4 (pH 7). A solar simulator (Lot-Oriel, 300 W Xe-arc lamp) was used to irradiate the sample through a quartz window integrated into the cell. The irradiance of the lamp, at the distance of the photocathode from the lamp (4.5 cm), was 385 mW cm^{-2}. Electrolyte containers were connected to each cell compartment through a peristaltic pump.

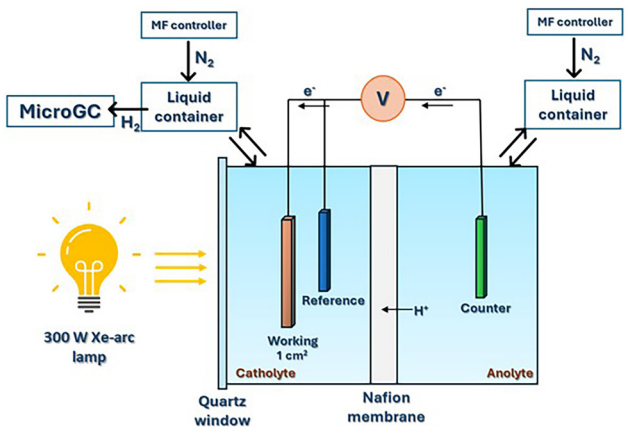

Fig. 2 Scheme of the set-up, including the photo-electrochemical (PEC) cell, the light source (300 W Xe-arc lamp) and the gas inlet and outlet connections.

The chronoamperometric (CA) analysis was performed at a fixed potential of −0.68 V *vs.* RHE in 0.1 M Na_2SO_4 under a continuous flow of N_2 using the solar simulator, equipped with various filters to cut out different ranges of wavelengths, for the irradiation of the samples. The filters used in this study were: the AM 1.5 G filter, which simulates the standard solar irradiation on Earth (with the UV part only about 4% of the entire spectrum), the UV-C blocking filter, and the UV B/C blocking filter. The samples were exposed to 30-second ON and OFF cycles of irradiation, during which the current density increased and then quickly returned to its initial value when the light was turned off showing high reproducibility. If not specified, in all experiments three cycles at open spectrum (and the last) were performed at the beginning.

The cyclic voltammetry (CV) was conducted over the potential range of +0.62 V to −0.88 V *vs.* RHE, at a scan rate of 10 mV s^{-1}, for 10 cycles.

The electrochemical impedance spectroscopy (EIS) analysis was performed in the frequency range from 10 000 Hz to 0.1 Hz, with an amplitude of $0.01V_{rms}$ at the applied potential of −0.68 V *vs.* RHE, the same as the catalytic tests, in dark and under light irradiation. The Zview® software was used to fit the data with the proper equivalent circuit.

The photo-electrocatalytic tests were carried out in the cell described above, by applying −0.68 V *vs.* RHE for 3 hours, with a lamp irradiance of 385 mW cm^{-2}. The high-intensity, open-spectrum regime was intentionally chosen to maximize the performance facilitating a direct comparison between the different ferrites to better understand the role of doping. Hydrogen production during water photo-electrolysis was quantified using a Gas Chromatograph (MicroGC GCX Pollution) equipped with a thermal conductivity detector (TCD). The tests were preceded by 30 minutes of N_2 purging with a flow rate of 24.4 mL min^{-1}, which was maintained throughout the tests. The electrocatalytic tests (in dark) were performed under the same conditions as the photo-electrocatalytic tests. 12 hours PEC stability tests of the Cu75Co25Fe and Cu95Zn5Fe samples were carried out in the same operational conditions of the PEC tests.

The potential values were converted from V *vs.* Ag/AgCl (3 M KCl) to V *vs.* RHE using the following equation:

$$E_{(RHE)} = E_{\left(\frac{Ag}{AgCl}\right)} + 0.059\,pH + 0.21\,V. \quad (2)$$

The following formula was used to determine Faradaic Efficiency (F.E.) where n is the number of electrons involved in the reduction process (*i.e.*, 2), F is the Faraday constant (96 485 C), m is the total amount (moles) of hydrogen produced during the process (3 h of reaction) and Q_{eff} is the charge determined from the measured current:

$$FE\,(\%) = \frac{nFm}{Q_{eff}} \times 100. \quad (3)$$

Results and discussion

Morphological, structural, physicochemical, and magnetic characterizations of magnetic ferrite systems

Fig. 3 reports the structural characterization (XRPD) of the bare ferrite systems, namely the bare Cu ferrite (Cu100Fe), the bare Co ferrite (Co100Fe), and the bare Zn ferrite (Zn100Fe). The XRPD analysis revealed the typical peaks due to the spinel crystal structure. In particular, in the case of Cu100Fe, the XRPD pattern shows the main relevant reflections at 2θ = 30.2° (220), 35.5° (311), 37.2° (222), 43.2° (400), 53.6° (422), 57.1° (511), 62.7° (440), 66.0° (531), and 75.2° (533), corresponding to the $CuFe_2O_4$ crystal phase (card number 01-077-0010, ICDD).[30] Moreover, the presence of extra signals at 2θ = 35.6° (−111), 38.8° (111), 48.7° (−202), 58.4° (202), 61.6° (−113), 68.2° (220), and 75.3° (−222) can be associated to the tenorite CuO monoclinic crystal phase (card number 01-080-1268, ICDD).[31] In the case of Co100Fe, the XRPD pattern shows the main relevant reflections at 2θ = 30.1° (104), 35.4° (113), 37.0° (006), 43.1° (024), 53.4° (214), 56.9° (125), 62.5° (208), and 75.0° (226) belonging to the $CoFe_2O_4$ crystal phase (card number 01-079-1744, ICDD).[32] Finally, in the case of Zn100Fe, the signals at 2θ = 30.0° (220), 35.3° (311), 36.9° (222), 42.9° (400), 53.2° (422), 56.7° (511), 62.2° (440), and 73.6° (533), corresponded to the $ZnFe_2O_4$ crystal phase (card number 03-065-3111, ICDD).[33]

As expected, the three magnetic ferrite systems show similar XRPD patterns, with slight shifts in the peak positions, which are mainly attributed to differences in term of ionic radius of the metallic species involved (*i.e.*, rCu^{2+} = 0.73 Å, rCo^{2+} = 0.63 Å, and rZn^{2+} = 0.75 Å) and/or in the degree of inversion of the ferrite, reflecting the distribution of cations between octahedral and tetrahedral sites.[34,35] Such difference in term of ionic radius affects both the lattice parameters and the cations distribution within the crystal structure (*vide infra*).

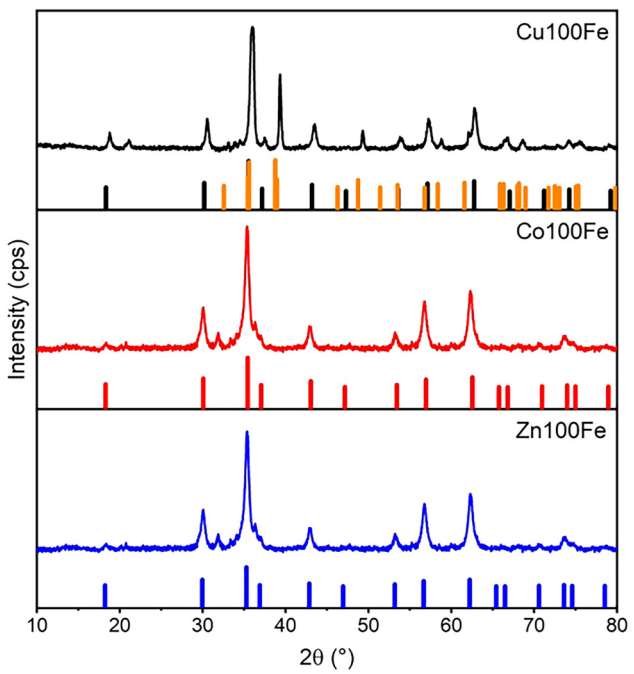

Fig. 3 XRPD patterns of bare ferrites, namely: Cu100Fe (top, black), Co100Fe (middle, red), and Zn100Fe (bottom, blue). XRPD reference patterns: $CuFe_2O_4$ (01-077-0010, black), CuO (01-080-1268, orange), $CoFe_2O_4$ (01-079-1744, red), and $ZnFe_2O_4$ (03-065-3111, blue).

Fig. 4 reports structural (XRPD) characterization of Co-substituted (Fig. 4a) and Zn-substituted (Fig. 4b) Cu ferrite systems. In general, the spinel crystal structure, characteristic of the three bare magnetic ferrite systems here investigated, has been retained in all cases. However, the Co- and Zn-doping generated a slight shift of the main signals of Cu ferrite, thus confirming the incorporation of either Co or Zn ions within its crystal structure. Moreover, similarly to the bare Cu ferrite (Cu100Fe), in all cases it was observed the formation of a secondary phase attributed to CuO. Interestingly, the CuO XRPD signals intensities gradually decrease with increasing the dopants concentration (*i.e.*, either Co or Zn ions), thus suggesting that the insertion of both Co^{2+} and Zn^{2+} (and the consequent relative Cu^{2+} content reduction) seems affecting the CuO secondary phase formation.[36]

Table S2 (SI) reports the lattice parameters and the crystallite average sizes of the cubic unit cell calculated for all magnetic ferrite systems. Among the bare ferrite systems, the Cu100Fe sample exhibits lower lattice parameters (and thus also a reduced lattice volume) compared to both Co100Fe and Zn100Fe systems. Interestingly, in the case of Co-substituted Cu ferrite systems, a gradual reduction of the lattice parameters can be attained by increasing the relative Co content, possibly due to the smaller ionic radius of Co^{2+} compared to Cu^{2+} ions.[37] Conversely, in the case of Zn-substituted Cu ferrite, it is registered a significant increase of the Cu ferrite crystal lattice, probably due to the larger ionic radius of Zn^{2+} ions respect to Cu^{2+} ions, which can lead to a lattice distortion. However, according to the literature,[38] though Zn^{2+} ions tend to occupy the tetrahedral A-sites, at relatively high dopant degree Zn^{2+} ions may also start occupying the octahedral B-sites due to the saturation reached for the tetrahedral A-sites.[39] This phenomenon might be at the origin of the observed cell volume increase with increasing the nominal Zn content, also accompanied by a gradual increment of the cell lattice parameters according to the Vegard's law.[40]

Concerning the crystallites average size evaluation, both Cu100Fe and Zn100Fe exhibited similar value of *ca.* 17 nm, *i.e.*, being slightly higher compared to that attained by Co100Fe corresponding to *ca.* 15 nm. Regarding Co-substituted ferrite systems, an increase of the average crystallite sizes up to *ca.* 20–22 nm values has been attained with progressively increasing the Co-substitution, while an abrupt increment of the crystallite average size (up to *ca.* 26 nm) has been registered with the Cu50Co50Fe sample.

Conversely, among the Zn-substituted ferrite systems, a remarkable size contraction (*ca.* 12 nm) was observed with the lowest substituted Cu95Zn5Fe material, followed by a progressive average size increase along with the Zn content, with a

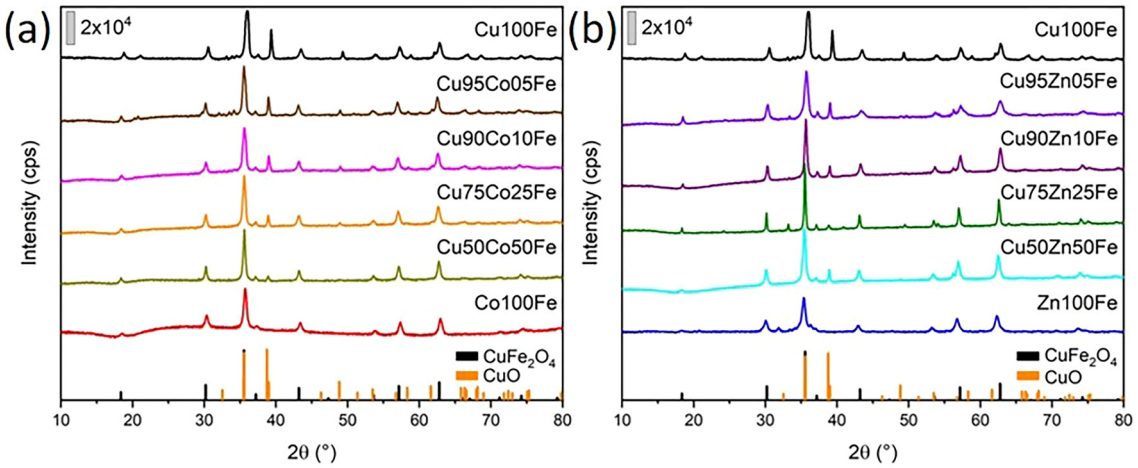

Fig. 4 XRPD patterns of partially substituted ferrite systems. (a, Left) Co-substituted Cu ferrite systems, namely: Cu100Fe (black), Cu95Co5Fe (brown), Cu90Co10Fe (magenta), Cu75Co25Fe (orange), Cu50Co50Fe (dark yellow), and Co100Fe (red). (b, Right) Zn-substituted Cu ferrite systems, namely: Cu100Fe (black), Cu95Zn5Fe (violet), Cu90Zn10Fe (purple), Cu75Zn25Fe (olive green), Cu50Zn50Fe (cyan), and Zn100Fe (blue). XRPD reference patterns: $CuFe_2O_4$ (01-077-0010, black), and CuO (01-080-1268, orange).

maximum value of *ca*. 55 nm being unexpectedly shown by the Cu75Zn25Fe sample.

SEM images of bare and differently substituted ferrite systems are reported in Fig. 5 and 6, respectively. In the case of bare Cu100Fe sample (Fig. 5a), it has been registered a heterogeneous morphology with co-presence of sub-rounded particles in the 40–600 nm range associated to Cu ferrite, and large anisotropic structures (several microns long, and *ca*. 500 nm thick) probably related to the CuO secondary phase,[41,42] in agreement with XRPD results. Differently, Co100Fe sample revealed a more homogeneous morphology mainly composed by micrometric particles with rounded edges, along with aggregates of nanoscopic particles (Fig. 5b), whereas Zn100Fe showed a homogeneous morphology composed by rod-like particles (several microns long, and *ca*. 100–500 nm thick) (Fig. 5c). In this latter case, the Zn100Fe anisotropic morphology can be attributed to the preferential growth of Zn ferrite systems along certain crystallographic directions. This is probably due to the preferential tendency of Zn^{2+} ions of occupying the tetrahedral A-site positions, thus favoring the formation of anisotropic crystals.[43] On the contrary, since Co^{2+} ions can occupy both the tetrahedral A-sites and the octahedral B-sites of the spinel crystal structure, in the case of Co100Fe sample this leads to a more homogeneous distribution of the species and the formation of more compact spheroidal particles.[44]

Interestingly, both Co- and Zn-substituted ferrite systems exhibited a drastic morphology variation, depending on both the chemical nature and the relative amount of the chosen dopant, replacing Cu in the crystal lattice. In particular, substituted systems with relatively low Co content (5–10%; Fig. 6a and b) show the co-presence of aggregates of nanoparticles together with anisotropic structures attributable to CuO, whereas at high Co content (25–50%; Fig. 6c and d) it has been registered the formation of concretion structures, as in Co100Fe sample. In the case of substituted systems with relatively low Zn content (5–10%; Fig. 6e and f), the formation of micrometric aggregates has been registered. At high content of Zn (25–50%; Fig. 6g and h), instead, the morphology is characterized by co-presence of structures with both rounded and angular edges, together with a drastic reduction of CuO-attributed nanorods' amount, in accordance with the trend registered during the XRPD analysis. However, differently from what observed in the case of Co-substituted ferrite systems, the

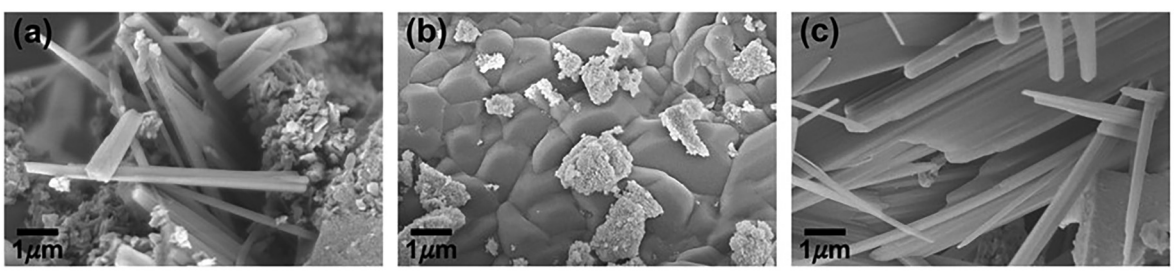

Fig. 5 SEM micrographs of bare ferrite systems namely: Cu100Fe (a, left), Co100Fe (b, middle), and Zn100Fe (c, right). Micrographs were collected at the same magnifications (30k×).

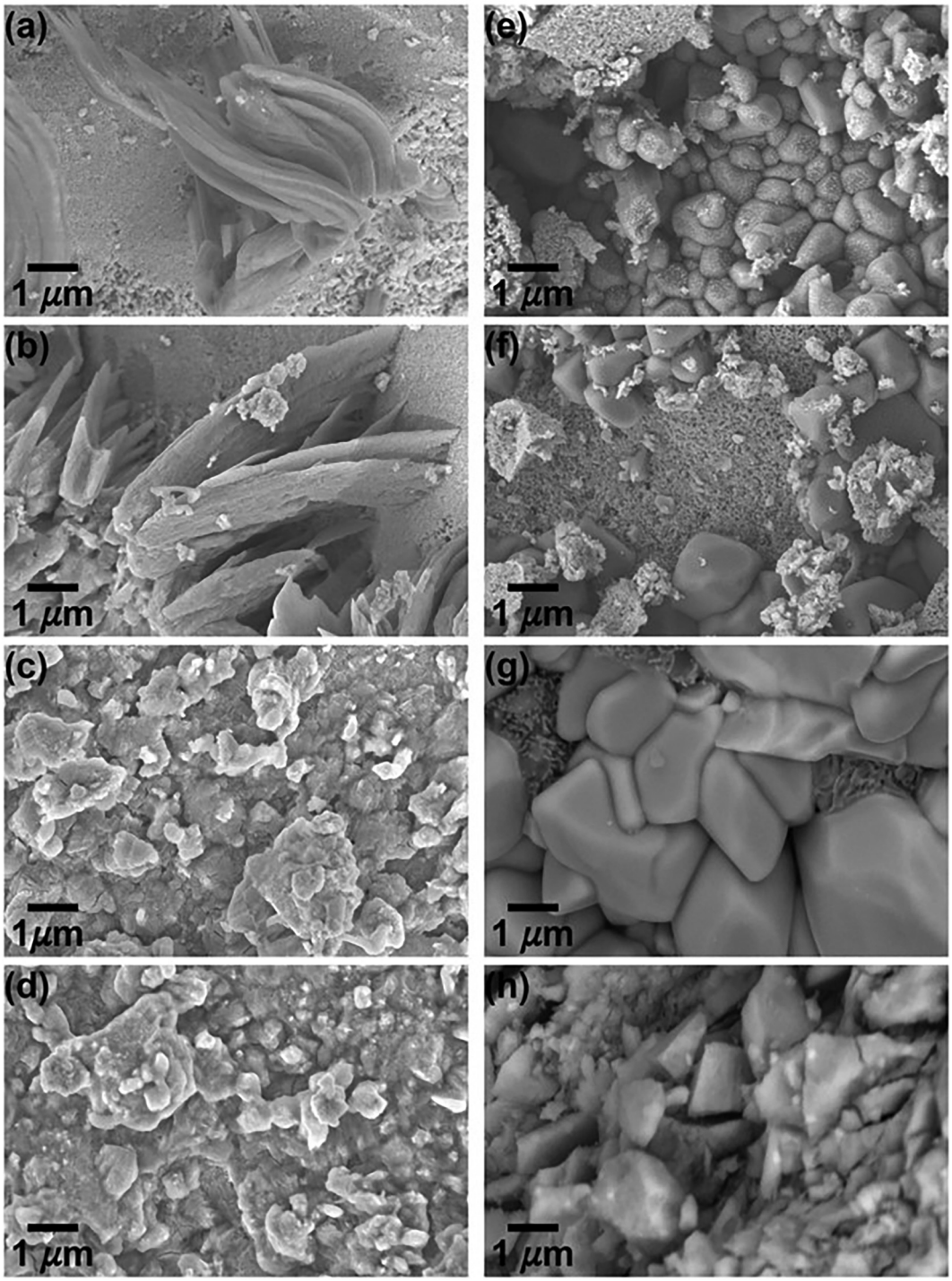

Fig. 6 SEM micrographs of Co-doped (left) and Zn-doped (right) Cu ferrite systems, namely: (a) Cu95Co5Fe, (b) Cu90Co10Fe, (c) Cu75Co25Fe, (d) Cu50Co50Fe, (e) Cu95Zn5Fe, (f) Cu90Zn10Fe, (g) Cu75Zn25Fe, (h) Cu50Zn50Fe. Micrographs were collected 30k× magnifications.

Zn-substituted ones do not show any similarity with the morphology exhibited by the bare Zn ferrite. This morphological phenomenon could be due to the change in preferential site occupancy by Zn^{2+} ions, starting to occupy both tetrahedral A-sites and octahedral B-sites when added at relatively high content.[45]

Magnetic properties of all ferrite systems were evaluated by means of magnetization curves measured at RT as reported in Fig. 7, whereas the numerical values of the identified fundamental magnetic parameters are summarized in Table 1.

All the bare ferrite systems exhibit superparamagnetic behaviors, with Co100Fe sample showing a hint of hysteresis (thus

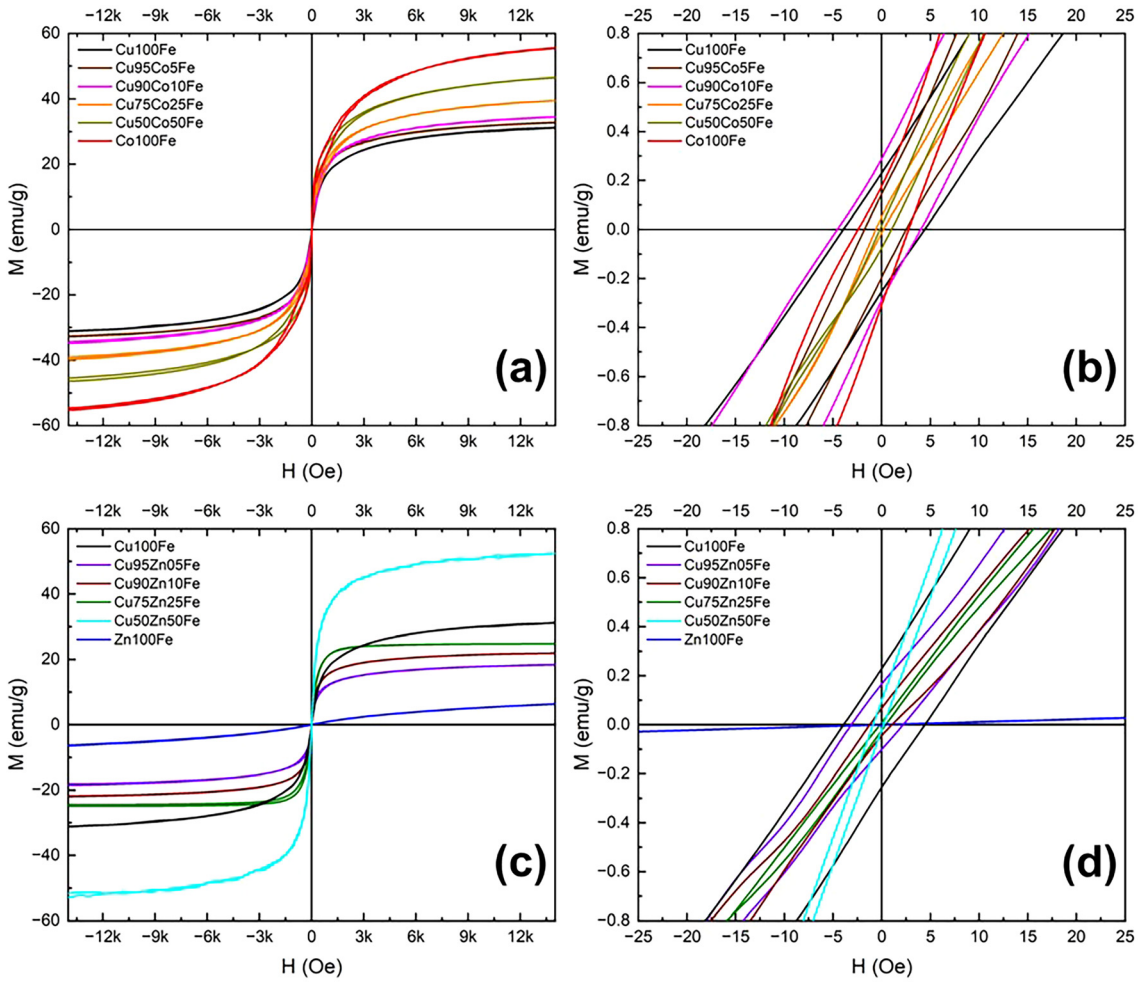

Fig. 7 Magnetization curves *M vs. H* of magnetic ferrite systems. (a) Comparison between bare Cu and Co ferrites with Co-substituted Cu ferrite systems, namely: Cu100Fe (black), Cu95Co5Fe (brown), Cu90Co10Fe (magenta), Cu75Co25Fe (orange), Cu50Co50Fe (dark yellow), and Co100Fe (red). (b) Magnetization curves enlargement area to highlight the middle section of the hysteresis loop of panel (a). (c) Comparison between bare Cu and Zn ferrites with Zn-substituted Cu ferrite systems, namely: Cu100Fe (black), Cu95Zn5Fe (violet), Cu90Zn10Fe (purple), Cu75Zn25Fe (olive green), Cu50Zn50Fe (cyan), and Zn100Fe (blue). (d) Magnetization curves enlargement area to highlight the middle section of the hysteresis loop of panel (c).

Table 1 Magnetic properties for both bare and substituted magnetic ferrite systems measured at RT

Samples	M_s (emu g^{-1})	H_c (Oe)	M_r (emu g^{-1})
Cu100Fe	31.27	4	0.23
Co100Fe	55.57	3	0.22
Zn100Fe	6.51	<1	0.27
Cu95Co5Fe	32.90	2	0.17
Cu90Co10Fe	34.78	4	0.27
Cu75Co25Fe	39.72	<1	0.04
Cu50Co50Fe	46.61	<1	0.06
Cu95Zn5Fe	18.51	3	0.14
Cu90Zn10Fe	22.02	1	0.05
Cu75Zn25Fe	24.85	<1	0.01
Cu50Zn50Fe	53.06	<1	0.09

indicating a certain level of ferrimagnetism), whereas Zn100Fe sample shows a very weak magnetic response. As indicated in Table 1, Co100Fe exhibits the highest value of saturation magnetization (M_s) among the analyzed samples (with *ca.* 56 emu g^{-1}), followed by Cu100Fe (with *ca.* 31 emu g^{-1}), and Zn100Fe (with only *ca.* 6 emu g^{-1}). Concerning both coercivity (H_c) and remnant magnetization (M_r) values, all bare ferrite systems exhibit almost negligible values, in accordance with their superparamagnetic behaviors.

Regarding the Cu ferrites doped with either Co or Zn, the experimental results reveal a progressive increase in the M_s with increasing the dopant concentration. In particular, samples doped with Co^{2+} exhibit an increase of the M_s values from *ca.* 33 emu g^{-1} for Cu95Co5Fe to *ca.* 47 emu g^{-1} for Cu50Co50Fe. These findings confirm that even low Co content (5%) significantly affect the M_s respect to the bare $CuFe_2O_4$ (Cu100Fe), primarily due to the substitution of Cu^{2+} with Co^{2+} ions, which possess a higher magnetic moment and enhance A–B super exchange interactions within the spinel structure.[46]

Opposite to this, when Cu100Fe is doped with Zn^{2+} it was observed a decrease in the M_s values from *ca.* 31 emu g^{-1} for Cu100Fe to *ca.* 18 emu g^{-1} for Cu95Zn5Fe, this could be attributed to the non-magnetic nature of Zn that dilutes the ferrimagnetic contribution due to Fe^{3+} cations.[47] However, quite surprisingly as Zn^{2+} content increases also M_s values increase, even if they still remained lower than the Cu100Fe one, except for the Cu50Zn50 sample, whose M_s reached 53 emu g^{-1}, which is higher than that of Cu100Fe.

Interestingly, Hammad *et al.*[37] investigated the effect of Zn^{2+} substitution in $CuFe_2O_4$ (*i.e.*, $Cu_{1-x}Zn_xFe_2O_4$), registering the increase of M_s values when x is in the 0.2–0.6 range, followed by a decrease when x is in the 0.8–1.0 range. Authors reported that the initial increment was attributed to changes in the distribution of ions within the $CuFe_2O_4$ lattice, where Fe^{3+} ions are evenly distributed between tetrahedral A-sites and octahedral B-sites positions, whereas Zn^{2+} ions preferentially tends to occupy the tetrahedral A-sites. This selective occupation reduces the magnetic moment of the A-sites, thereby increasing the net magnetization and, consequently, the M_s. On the contrary, at high concentration of Zn^{2+} ions some of them also migrates to the octahedral B-sites, thus reducing the overall M_s values.

Photo-electrochemical characterizations of magnetic ferrite systems

To evaluate the response at different wavelength regions, chronoamperometric (CA) measurements were performed and the results are reported in Fig. 8. Upon irradiation, a strong photocathodic response is observed, as evidenced by the registration of an intense current density increase (in absolute value). The measurements were performed both under the full spectrum of the UV–visible lamp and with optical filters (AM1.5G, UVC blocking filter, and UVB/C blocking filter). In particular, the AM1.5G filter, which reproduces the solar spectrum at the Earth's surface, caused a distinct photocurrent response. This behavior is consistent with the absorption profile of the ferrite catalysts in the visible region, confirming their suitability for solar-driven photo-electrocatalytic applications.[48] Since the dark current density differs among the samples, probably due to side reactions,[48] the relative increase with respect to the dark baseline was calculated, and the

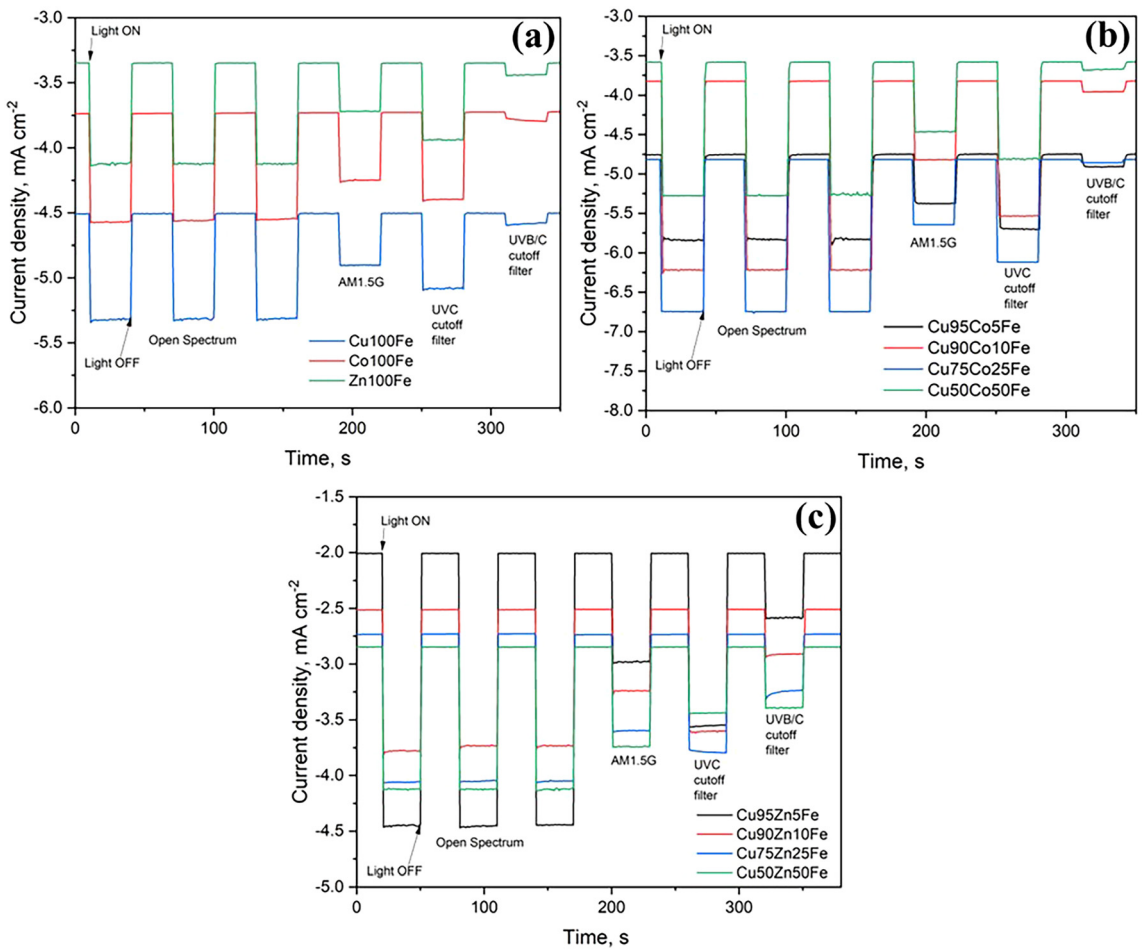

Fig. 8 Chronoamperometric measurements of (a) bare ferrite systems, (b) Co-substituted and (c) Zn-substituted Cu ferrite systems. Signals were recorded in 0.1 M Na_2SO_4, at −0.68 V *vs.* RHE; the light was switched ON and OFF every 30 s.

results in percentages are reported in Table S3 (SI). While in the case of the bare ferrite systems the difference in the increment percentages is minor, with the Co–Cu ferrite systems and the Zn–Cu ferrite systems the differences are more significant, with an increment of the photocurrent at open spectrum of 62% for the Cu90Co10Fe sample and 116% in the case of Cu95Zn5Fe.

Electrochemical impedance spectroscopy (EIS) was performed to evaluate charge transfer phenomena occurring at the photo-electrodes/electrolyte interface and the results attained during tests performed under light irradiation are reported in Fig. 9. EIS results acquired in dark conditions are collected in Fig. S1 (SI).

Specifically, Fig. 9a–c show the comparison of Nyquist plots obtained for the ferrite systems with the application of light, with the dots representing the experimental data, acquired using the testing conditions (−0.68 V *vs.* RHE, 0.1 M Na_2SO_4) and the lines representing the fitting curves calculated by the Zview® software using the equivalent two-constant circuit model shown in Fig. 9d, commonly employed to describe semiconductor/electrolyte systems.[49] The equivalent circuit is composed of three main contributions: (i) a series resistance (*Rs*), accounting for ohmic losses related to the FTO substrate and electrical contacts; (ii) the high frequency contribution, represented by *R*p1 and CPE1, associated with the charge transport within the ferrite bulk and the space-charge region, and is strongly influenced by composition and crystallinity; and (iii) the low frequency contribution, described by *R*p2 and CPE2, which reflects the charge transfer processes and capacitive effects at the ferrite/electrolyte interface, influenced by surface morphology and electrochemically accessible surface area.[49,50]

Table S4 (SI) summarizes the values calculated from the fitting. Starting from the values of *Rs*, they indicate relatively small ohmic losses across the FTO/ferrite interface, in the range of 16–44 Ω, with Cu50Zn50Fe having the highest resistance (44.14 Ω). The differences among *R*p1 highlight the variations in bulk charge transport in the ferrite systems, with the bare Cu ferrite and the bare Co ferrite exhibiting low *R*p1 values (12.6 and 6.3 Ω, respectively), while the Zn- and Co-doped Cu ferrites exhibit higher *R*p1, suggesting a stronger contribution from bulk recombination. The interfacial resistance *R*p2, related to charge transfer at the ferrite/electrolyte junction, is in the range between *ca.* 6 Ω (Cu75Co25Fe) and

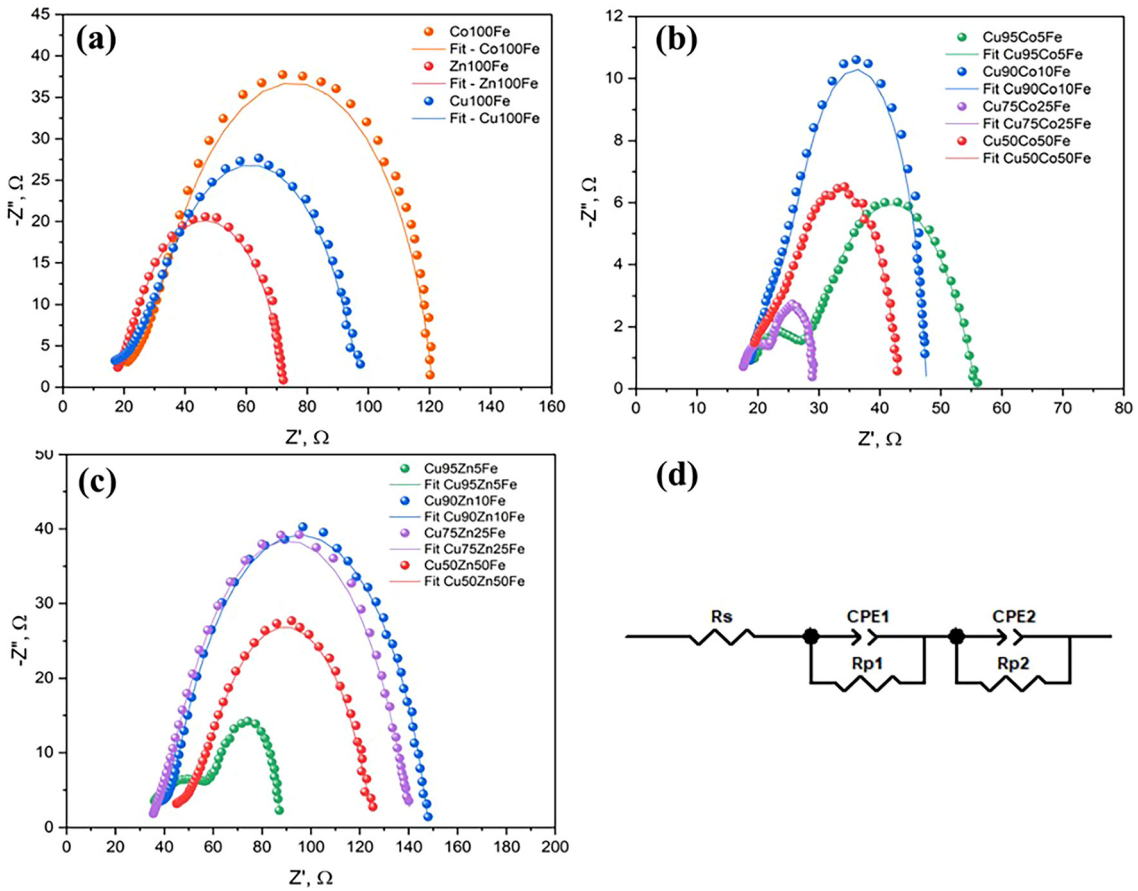

Fig. 9 Nyquist plots under light irradiation for the bare ferrite systems (a), Co substituted Cu ferrite systems (b), Zn substituted Cu ferrite systems (c), with the dots representing the raw data (recorded applying −0.68 V *vs.* RHE, frequency range from 10 000 Hz to 0.1 Hz, with an amplitude of $0.01V_{rms}$ and with the application of light) and the lines representing the fitting performed by using the two-constant circuit model shown in (d).

over 100 Ω (Cu90Zn10Fe). Lower *R*p2 values correspond to more favorable interfacial charge transfer kinetics, while higher values suggest slow surface reactions.[51] In this regard, Co-doped Cu ferrites generally display lower *R*p2 compared to Zn-doped samples, indicating that Co addition enhances charge-transfer properties. Thus, the addition of Co and Zn in the Cu ferrite has beneficial effects in the overall photo-electrocatalytic characteristics of the material: Co-containing ferrites favor lower charge-transfer resistance at the electrode/electrolyte interface, while Zn incorporation strongly affects the bulk dielectric properties, while maintaining a low charge-transfer resistance when added in a small quantity.

Fig. 10a–c show the CV curves of the samples under light application, recorded at 10 mV s^{-1}. Each panel has a zoomed-in region around −0.6 V to −0.4 V *vs.* RHE, to clearly show the differences in terms of HER onset potential. In general, there is an increase in the cathodic current starting at −0.4 to −0.6 V *vs.* RHE, due to the hydrogen evolution reaction (HER).[52]

The onset potential values for HER were estimated with the tangent method[53] from the CVs for every sample and the values are listed in Table S5 (SI). Among the bare ferrites, Cu100Fe exhibits the most positive onset potential (−0.58 V *vs.* RHE), while Zn100Fe and Co100Fe show slightly more negative values (−0.62 V and −0.61 V, respectively). This suggests that Cu-based ferrite favors the initiation of photocathodic processes at lower overpotentials compared to Co- and Zn-bare ferrites.

In the Co-doped Cu ferrite systems, the progressive incorporation of Co shifts V_{onset} towards more negative values, reaching −0.67 V for Cu50Co50Fe. Cu95Co5Fe (−0.63 V), Cu90Co10Fe (−0.66 V), Cu75Co25Fe (−0.64 V) show intermediate behavior, pointing to a non-linear effect of Co incorporation on band alignment and charge-transfer kinetics, as suggested also with the R_{p2} values.

Conversely, the Zn-doped Cu ferrites displays a different trend. While Cu95Zn5Fe, Cu75Zn25Fe and Cu50Zn50Fe present onset values like those of the bare ferrites (−0.59 to −0.62 V), the Cu90Zn10Fe sample stands out with a significantly more positive onset potential (−0.45 V *vs.* RHE), while showing the highest value of *R*p2, suggesting an earlier photo response, but a less efficient interfacial charge transport.[54]

This indicates that limited Zn incorporation strongly enhances the ease of photocathodic activity, possibly due to favorable modifications of the electronic structure and band positions. However, higher Zn contents (Cu75Zn25Fe and Cu50Zn50Fe) have onset values comparable to bare Cu– or Zn–ferrites, suggesting that the beneficial effect is maximized at

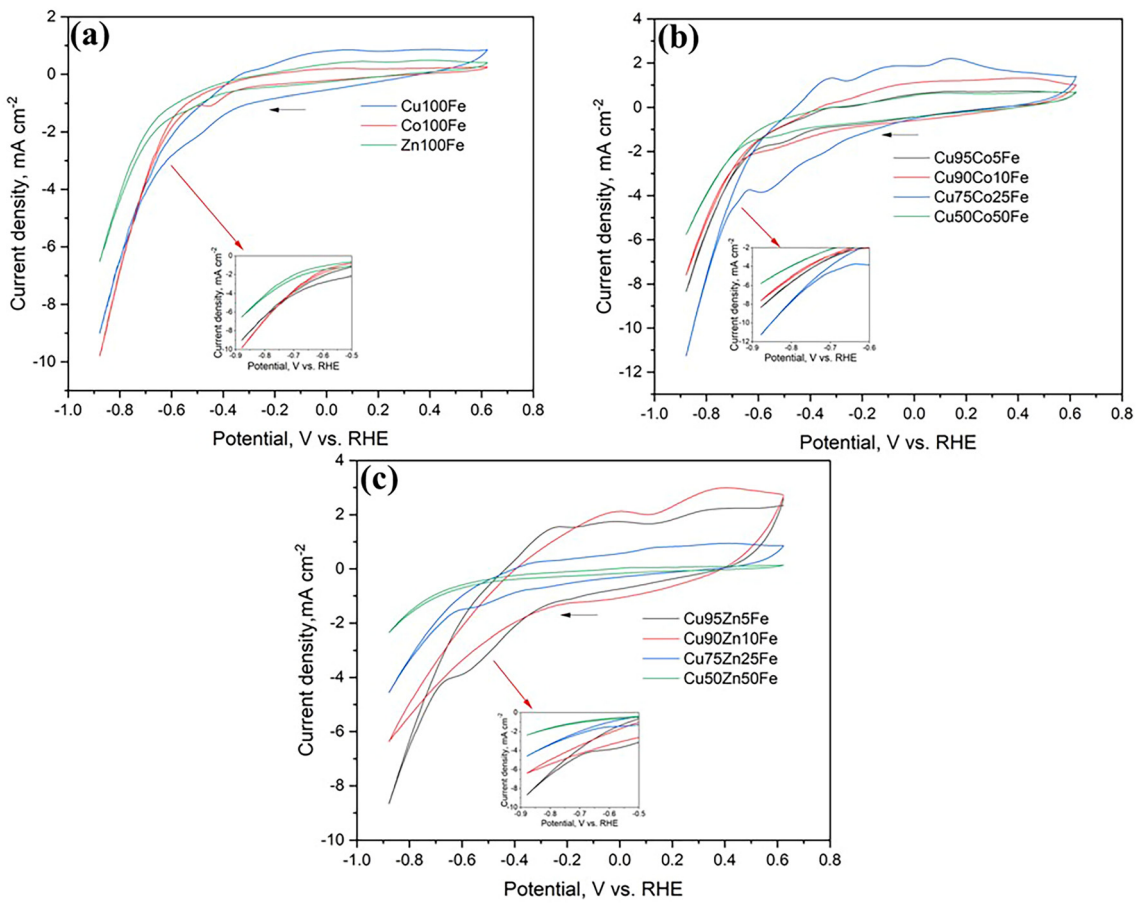

Fig. 10 Cyclic voltammetry (CV) profiles for the bare ferrite systems (a), Co substituted Cu ferrite systems (b), Zn substituted Cu ferrite systems (c), recorded at 10 mV s^{-1} in Na_2SO_4 0.1 M with the application of light.

low Zn percentage, as suggested by the photocurrent measurement and EIS results. Overall, Cu100Fe and Cu90Zn10Fe have the most favorable onset potentials, facilitating photocathodic activation at less negative bias.

The Tafel slopes were extracted from the kinetically controlled region of the CV curves, selecting the overpotential range where the η *vs.* log j plot displays a linear behavior. The kinetics of Zn-modified samples are strongly dependent on the metal concentration, whereas for Co-modified samples the reaction kinetics are essentially unaffected by the metal loading, as evidenced by the results reported in Table S6 (SI). The electrochemically active surface area (ECSA) values are reported in the SI (Table S7).

The relatively narrow distribution of ECSA values indicates good reproducibility of the deposition process, suggesting that variations in catalytic performance are not primarily driven by differences in the electrochemically active surface area.

Photo-electrochemical testing

The effect of the different ferrite-based samples was investigated in the process of water photo-electrolysis using the three-electrode cell described in Fig. 2. The hydrogen production (mmol g^{-1}), Faradaic Efficiency (F.E. %) and the average current density normalized with the ECSA values attained during either PEC (photo-electrocatalytic) or EC (electrocatalytic) tests have been compared in Fig. 11 and Table S8 (SI). The PEC and EC tests for each catalyst were performed for three hours at the same applied potential to have a direct comparison. The beneficial effect of light and thus the photoactivity of the systems are evident, as all samples exhibit a higher hydrogen production under illumination compared to dark conditions.

Even if this study aims at finding a comparative evaluation of dopants' effect rather than a fundamental mechanistic investigation, in the following discussion the present authors tried to provide an interpretation of the catalytic performances of catalysts based on the comparison with the scientific literature.

Hence, in neutral media, the HER consists in a process following these reactions, in which M is the surface site of the catalyst and M–H is the hydrogen absorbed on the site:[55–57]

$$H_2O + e^- + M \rightarrow M\text{–}H + OH^- \quad (4)$$

$$H_2O + e^- + M\text{–}H \rightarrow H_2 + OH^- + M \quad (5)$$

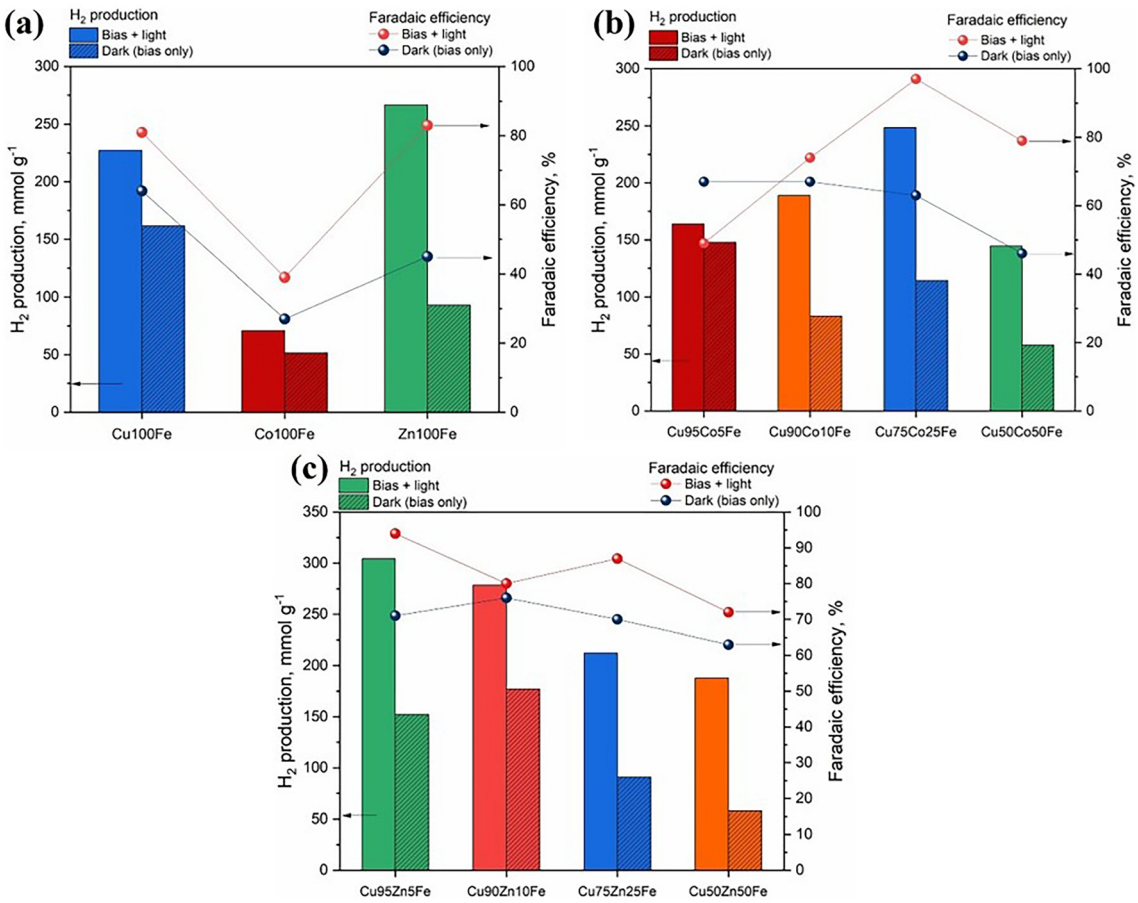

Fig. 11 Hydrogen production (bars) and F.E. (line and dot) of the PEC (bias + light) and EC (bias only) water splitting for the bare ferrite systems (a), Co substituted Cu ferrite systems (b), Zn substituted Cu ferrite systems (c). Reaction conditions: 0.1M Na_2SO_4, −0.68 V *vs.* RHE, time: 3 hours, full spectrum light irradiation (385 mW cm^{-2}).

$$2M\text{–}H \rightarrow 2M + H_2 \quad (6)$$

After the first step, the Volmer reaction (eqn (4)), the intermediate M–H could go through the electrochemical Heyrovsky step (eqn (5)) or the chemical Tafel step (eqn (6)).[58] The kinetics of the HER process depend on the M–H bond, whose strength should be not too weak nor too strong to promote the HER, in accordance with Sabatier's principle.[59,60] For an in-depth study related to the reaction mechanism involving the employment of spinel ferrites in PEC process for hydrogen evolution, please refers to the studies by Qin *et al.*,[61] and Zhang *et al.*[62]

Among the bare ferrite systems (Fig. 11a), Zn100Fe stands out for the highest hydrogen production in the PEC test (266.8 mmol g^{-1}), with a F.E. of 83%. Cu100Fe shows intermediate performance, with H_2 productivity of 227.4 mmol g^{-1} and 81% F.E., indicating that although charge carriers contribute to hydrogen formation, side reactions, likely OH^- adsorption/oxidation also can occur.[63] Co100Fe has the lowest activity, both in terms of H_2 productivity and F.E. confirmed by the higher *R*p2 value obtained from the EIS results. This could result from an excessively strong M–H binding on Co sites, which traps intermediates and slows hydrogen release through (eqn (5)) or (eqn (6)). In terms of performances, the ferrites thus follow this order: Zn100Fe > Cu100Fe > Co100Fe. This suggests that Zn incorporation produces an optimal M–H interaction, favoring both the Volmer step and efficient desorption *via* Heyrovsky/Tafel routes. The exceptional catalytic behavior of Zn ferrite system in well in line with the EIS results (low value of resistances). Observing the PEC results, the Cu ferrite systems doped with Co show a very interesting behavior, indicating a clear correlation between the Co content and the catalytic performances (Fig. 11b). As the Co concentration increases (from 5 to 25%), hydrogen production also increases, reaching the maximum value (248.7 mmol g^{-1}) using the Cu ferrite modified with 25% of Co, with F.E. of 97% (the highest among all samples analyzed). However, as the Co content increases further (to 50%), the H_2 evolution decreases, though it remains at a significant level of about 144.5 mmol g^{-1}, confirming that a high percentage of Co strengthens M–H too much, hindering H_2 desorption, as suggested for the results obtained with the bare Co100Fe sample. This trend is consistent with the charge transfer resistance values of the samples (see *R*p2 in Table S4). It can therefore be stated that there is an optimal amount of Co that can allow synergistic interaction with Cu sites, *i.e.*, Cu75Co25Fe sample outperforming the Cu100Fe one.

Regarding the performances of the Zn-doped Cu-ferrites in the photo-electrochemical test (Fig. 11c), the hydrogen production decreases as the Zn percentage increases, with a maximum in production for the Cu95Zn5Fe of 304.3 mmol g^{-1} and a F.E. of 94%. These results are in good agreement with the EIS results, which reveal the lowest resistance value with the Cu95Zn5Fe sample. Increasing the Zn content beyond 10% (Cu90Zn10Fe, Cu75Zn25Fe, Cu50Zn50Fe) lowers both the production and efficiency, indicating that excessive Zn weakens M–H interactions.

During long-term (12 hours) tests (Fig. S2, SI) Cu95Zn5Fe and Cu75Co25Fe catalysts maintained a stable current density, thus indicating the good durability of the photoelectrodes, with a total hydrogen production of 875.3 mmol g^{-1} and 1532.5 mmol g^{-1}, respectively. XRPD analyses (Fig. S3, SI) performed before and after the stability tests revealed no appreciable variations in terms of peaks' position and/or intensity, thus indicating that no phase transformation occurs during operation.

These results are in line with the work of Rodriguez–Rodriguez and collaborators, testing Zn, Ni, and Co ferrites for photocatalytic hydrogen evolution from methanol solutions. They observed a similar photocatalytic activity trend (Zn > Co), attributing it to the conduction band energies of the materials.[63] These results are very promising, since, although there are several studies involving the use of ferrites for photocatalytic water splitting,[64–68] the best results reported, showed a hydrogen evolution of 26 mmol g^{-1}_{cat} with Ni–Zn4 material.[68]

Furthermore, one last point that needs attention is the role due to magnetism. In fact, according to the literature, magnetism may promote the PEC process efficiency by generating Lorentz forces able to suppress the recombination of electron–hole pairs photogenerated on the photocatalysts.[69] At the same time, the application of an external magnetic field may also promote the so-called spin selective effect, which consists in the preferential interconversion between two spin states (either singlet or triplet) occurring on intermediate species adsorbed on the catalysts surface, thus affecting the overall reaction pathways.[70] For instance, Niether *et al.*[71] reported that the application of an external magnetic field in presence of a magnet-sensitive catalyst might improve the electrocatalytic performances in HER and OER water splitting. However, in the present study, all PEC tests were performed in absence of any external magnetic field applied, and magnetic ferrites employed as catalysts are not permanent magnet (as clearly demonstrated by the magnetic characterization in Fig. 7), thus authors can exclude any catalytic role due to magnetism at the current experimental conditions adopted.

Conclusions

A series of magnetic ferrite systems based on $CuFe_2O_4$, $CoFe_2O_4$, $ZnFe_2O_4$, and their Co- and Zn-substituted $CuFe_2O_4$ analogues were successfully synthesized *via* a facile co-precipitation method and evaluated as photo-electrocatalysts for hydrogen evolution in neutral aqueous media. All materials crystallized in the spinel structure, with structural parameters and morphology evolving systematically with dopant type and concentration. Magnetic measurements confirmed that Co incorporation strengthened ferrimagnetic interactions, while Zn doping induced structural distortion and magnetic dilution.

Electrochemical and photo-electrochemical studies revealed that both Co and Zn substitutions significantly improved HER

performance compared to the pristine $CuFe_2O_4$. In particular, among Cu-substituted samples, Cu75Co25Fe achieved 97% F. E., while among the Zn-modified ferrites, Cu95Zn5Fe exhibited the highest hydrogen production (304.3 mmol g^{-1}) and the lowest interfacial resistance under illumination. The results demonstrate that the synergistic interplay between cation substitution, electronic configuration, and charge-transport properties drives the overall photo-electrocatalytic activity.

These results also confirm that partial replacement of Cu^{2+} with Co^{2+} or Zn^{2+} in $CuFe_2O_4$ represents an effective strategy to modulate the physicochemical and magnetic features of ferrites, optimizing their performance toward efficient, stable, and magnetically recoverable photo-electrocatalysts for sustainable hydrogen generation.

Author contributions

Luana De Pasquale (L. D. P.): investigation, formal analysis, data curation, writing – original draft, writing – review & editing. Tatiana Rodriguez-Flores (T. R. F.): investigation, formal analysis, data curation, writing – original draft, writing – review & editing. Daniele Valenzisi (D. V.): investigation, formal analysis, writing – review & editing. Falak Shafiq (F. S.): investigation, formal analysis, writing – review & editing. Roberto Scotti (R. S.): investigation, writing – review & editing. Francesco Tavella (F. T.): investigation, formal analysis, writing – review & editing. Matteo Cantoni (M. C.): investigation, formal analysis, writing – review & editing. Maria Vittoria Dozzi (M. V. D.): investigation, writing – review & editing, funding acquisition. Chiara Genovese (C. G.): methodology, validation, conceptualization, formal analysis, supervision, writing – review & editing, funding acquisition. Roberto Nisticò (R. N.): methodology, validation, conceptualization, formal analysis, supervision, investigation, resources, writing – original draft, writing – review & editing, funding acquisition.

Conflicts of interest

The authors declare that they have no known competing financial interests or personal relationships that could have appeared to influence the work reported in this paper.

Data availability

The supporting data has been provided as part of the supplementary information (SI). Supplementary information: compositional parameters; lattice parameters and crystallite average sizes; electrode preparation; current density percentage increment after exposure to different light irradiation conditions; Nyquist plots in dark conditions; resistance values measured by EIS fitting; V_{onset} for HER and Tafel slope calculated from CV curves; ECSA; average current density, hydrogen production and F.E. of the PEC and EC water splitting; stability tests; XRPD characterization before and after stability tests. See DOI: https://doi.org/10.1039/d5dt03018h.

Acknowledgements

This work received financial support from MUR (Italy) and the European Union – Next Generation EU, Mission 4, Component 1, CUP (H53D23004490001) through the PRIN Project MAPEC (N. 2022599NR3), and CUP (H53D23008000001) through the PRIN Project PERFECT (N. P2022TK9B9). R. N. would like to acknowledge the National Recovery and Resilience Plan (PNRR), Mission 2 "Green Revolution and Ecological Transition", Component 2 "Renewable Energy, Hydrogen, Network and Sustainable Mobility", Investment 3.5 "Hydrogen Research and Development", European Union – Next Generation EU – Ministry of Ecological Transition, project AMBITION. T. R. F. would like to acknowledge the Secreteria de Educacion, Ciencia, Tecnologia e Inovacion (Mexico City, Mexico) No. SECTEI/197/2024. Authors would like to acknowledge Dr Paolo Gentile (University of Milano-Bicocca, Italy) for the technical support during the SEM analysis.

References

1 S. Chamani, M. Khatamian, N. S. Peighambardoust and U. Aydemir, Microwave-assisted auto-combustion synthesis of binary/ternary Co_xNi_{1-x}ferrite for electrochemical hydrogen and oxygen evolution, *ACS Omega*, 2021, **6**, 33024–33032, DOI: 10.1021/acsomega.1c05183.

2 H. Belhadj, Y. Messaoudi, M. R. Khelladi and A. Azizi, A facile synthesis of metal ferrites (MFe_2O_4, M = Co, Ni, Zn, Cu) as effective electrocatalysts toward electrochemical hydrogen evolution reaction, *Int. J. Hydrogen Energy*, 2022, **47**, 20129–20137, DOI: 10.1016/j.ijhydene.2022.04.151.

3 X. T. Mai, H. H. Luc, P. D. Tran and L. T. Le, Sol-gel synthesis of copper ferrite spinel oxide and its use as catalyst for the H_2 evolution and CO_2 to acetate reduction reactions, *ChemistrySelect*, 2025, **10**, e00515, DOI: 10.1002/slct.202500515.

4 N. S. Porter, H. Wu, Z. Quan and J. Fang, Shape-control and electrocatalytic activity-enhancement of Pt-based bimetallic nanocrystals, *Chem. Res.*, 2013, **46**, 1867–1877, DOI: 10.1021/ar3002238.

5 R. V. Digraskar, V. S. Sapner, S. M. Mali, S. S. Narwade, A. V. Ghule and B. R. Sathe, CZTS decorated on graphene oxide as an efficient electrocatalyst for high-performance hydrogen evolution reaction, *ACS Omega*, 2019, **4**, 7650–7657, DOI: 10.1021/acsomega.8b03587.

6 C. Li and J.-B. Baek, Recent advances in noble metal (Pt, Ru, and Ir)-based electrocatalysts for efficient hydrogen evolution reaction, *ACS Omega*, 2020, **5**, 31–40, DOI: 10.1021/acsomega.9b03550.

7 B. Ruqia and S.-I. Choi, Pt and Pt–$Ni(OH)_2$ electrodes for the hydrogen evolution reaction in alkaline electrolytes and

their nanoscaled electrocatalysts, *ChemSusChem*, 2018, **11**, 2643–2653, DOI: 10.1002/cssc.201800781.

8 R. Jasrotia, A. Verma, A. V. Nidhi, J. Ahmed, M. Fazil, V. Khanna, S. Kumari, T. Ahmad, S. M. Alshehri and A. Kandwal, Nanocrystalline Co/Ga substituted $CuFe_2O_4$ magnetic nanoferrites for green hydrogen generation, *Int. J. Hydrogen Energy*, 2024, **52**, 1194–1205, DOI: 10.1016/j.ijhydene.2023.10.292.

9 S. Chamani, E. Sadeghi, N. S. Peighambardoust, F. Doganay, G. Yanalak, Z. Eroglu, E. Aslan, E. Asghari, O. Metin, I. H. Patir, U. Aydemir and M. Khatamian, Photocatalytic hydrogen evolution performance of metal ferrites/polypyrrole nanocomposites, *Int. J. Hydrogen Energy*, 2022, **47**, 32940–32954, DOI: 10.1016/j.ijhydene.2022.07.193.

10 R. Jabbar, S. H. Sabeeh and A. M. Hameed, Structural, dielectric and magnetic properties of Mn^{+2} doped cobalt ferrite nanoparticles, *J. Magn. Magn. Mater.*, 2020, **494**, 165726, DOI: 10.1016/j.jmmm.2019.165726.

11 S. Jabeen, M. Saleem, F. Mumtaz, S. Javed, M. Ali, M. Z. Khan, J.-H. Koh, A. Maqbool, A. H. Baluch, M. B. K. Niazig and I. Hussain, Coupling the power of spinel nanoparticles: dual-function metal ferrite catalysts for advanced piezo-photocatalytic and electrocatalytic water splitting, *J. Mater. Chem. A*, 2025, **13**, 29911–29929, DOI: 10.1039/D5TA01180A.

12 R. Parsons, The rate of electrolytic hydrogen evolution and the heat of adsorption of hydrogen, *Trans. Faraday Soc.*, 1958, **54**, 1053–1063, DOI: 10.1039/TF9585401053.

13 M. Ismael, A simple sol–gel method for the synthesis of Pt co-catalyzed spinel-type $CuFe_2O_4$ for hydrogen production; the role of crystallinity and band gap energy, *Fuel*, 2024, **359**, 130429, DOI: 10.1016/j.fuel.2023.130429.

14 K. J. Kim, J. H. Lee and S. H. Lee, Magneto-optical investigation of spinel ferrite $CuFe_2O_4$: observation of Jahn–Teller effect in Cu^{2+} ion, *J. Magn. Magn. Mater.*, 2004, **279**, 173–177, DOI: 10.1016/j.jmmm.2004.01.078.

15 M. Danish, A. Hussain, S. R. Shafqat, Z. A. Sandhu, K. M. Batoo, M. F. Ijaz, A. H. Bhalli and M. Fiaz, Multifunctional $CuFe_2O_4$ nanocomposites: 3D series-metal-based materials for hydrogen evolution reaction and supercapacitor applications, *Ceram. Int.*, 2025, **51**, 24989–24998, DOI: 10.1016/j.ceramint.2025.03.180.

16 R. Nivetha, C. Santhosh, P. Kollu, S. K. Jeong, A. Bhatnagar and A. N. Grace, Cobalt and nickel ferrites-based graphene nanocomposites for electrochemical hydrogen evolution, *J. Magn. Magn. Mater.*, 2018, **448**, 165–171, DOI: 10.1016/j.jmmm.2017.05.083.

17 K. Sathiyamurthy, C. Rajeevgandhi, S. Bharanidharan, P. Sugumar and S. Subashchandrabose, Electrochemical and magnetic properties of zinc ferrite nanoparticles through chemical co-precipitation method, *Chem. Data Collect.*, 2020, **28**, 100477, DOI: 10.1016/j.cdc.2020.100477.

18 A. Nasser, W. Bouslama, R. Nasser, A. S. Alahmari, A. Othmani, J. M. Song and H. Elhouichet, Structural characterization, dielectric behavior, AC conductivity analysis, and electrochemical performance of sol-gel synthesized zinc ferrite for advanced applications, *Ceram. Int.*, 2025, **51**, 37572–37582, DOI: 10.1016/j.ceramint.2025.06.009.

19 R. Nivetha and A. N. Grace, Manganese and zinc ferrite-based graphene nanocomposites for electrochemical hydrogen evolution reaction, *J. Alloys Compd.*, 2019, **796**, 185–195, DOI: 10.1016/j.jallcom.2019.05.021.

20 N. R. Manwar, R. G. Borkar, R. Khobragade, S. S. Rayalu, S. L. Jain, A. K. Bansiwal and N. K. Labhsetwar, Efficient solar photo-electrochemical hydrogen generation using nanocrystalline $CeFeO_3$ synthesized by a modified microwave assisted method, *Int. J. Hydrogen Energy*, 2017, **42**, 10931–10942, DOI: 10.1016/j.ijhydene.2017.01.227.

21 A. Wolcott, W. A. Smith, T. R. Kuykendall, Y. Zhao and J. Z. Zhang, Photoelectrochemical study of nanostructured ZnO thin films for hydrogen generation from water splitting, *Adv. Funct. Mater.*, 2009, **19**, 1849–1856, DOI: 10.1002/adfm.200801363.

22 S. Attia, N. Helaili, G. Rekhila, Y. Bessekhouad and M. Trari, Physical and photo-electrochemical properties of the spinel $SrFe_2O_4$: application to hydrogen production under visible light, *J. Mater. Sci.: Mater. Electron.*, 2022, **33**, 9976–9987, DOI: 10.1007/s10854-022-07989-1.

23 G. Rekhila, Y. Bessekhouad and M. Trari, Hydrogen evolution under visible light over the solid solution $NiFe_{2-x}Mn_xO_4$ prepared by sol gel, *Int. J. Hydrogen Energy*, 2015, **40**, 12611–12618, DOI: 10.1016/j.ijhydene.2015.07.109.

24 C. V. Tran, T.-D. Dang, V. D. Lai, G. T. Nguyen, B. T. Hoa, H. T. Nguyen, H. P. N. Thi, T. T. Nguyen and D. D. La, Self-assembly of porphyrin nanofiber on the surface $CuFe_2O_4$ nanoparticles: A novel photoanode for enhanced photoelectrochemical water splitting, *Fuel*, 2025, **380**, 133196, DOI: 10.1016/j.fuel.2024.133196.

25 M. Salman, M. Khan, S. Saleem, S. Ali, F. Hussain, R. Muhammad, A. Khesro, Abdullah and Y. Ling, Non-stoichiometric zinc ferrite nanostructures: Dielectric, magnetic, optical and photoelectrochemical properties, *Mater. Today Commun.*, 2021, **28**, 102662, DOI: 10.1016/j.mtcomm.2021.102662.

26 K. M. Amin, N. A. Eldeeb, Z. Gargar, I. M. A. Mohamed, M. Elsenety, M. H. Emara, A. Elkodous, M. M. Abouelela, P. A. Ibrahim, A. A. Ayed, H. N. Abdelhamid and H. A. Hamad, Ferrite-based nanomaterials for photocatalytic CO_2 reduction: Synthesis, properties, and mechanistic insights, *J. CO2 Util.*, 2025, **100**, 103175, DOI: 10.1016/j.jcou.2025.103175.

27 M. I. Diez-Garcia, T. Lana-Villarreal and R. Gomez, Study of copper ferrite as a novel photocathode for water reduction: Improving its photoactivity by electrochemical pretreatment, *ChemSusChem*, 2016, **9**, 1504–1512, DOI: 10.1002/cssc.201600023.

28 F. Germaninezhad, R. Hosseinzadeg, M. Tajbakhsh and A. Beitollahi, Copper ferrite nanoparticles: An effective and recoverable nanomagnetic catalyst for the synthesis of N,

N′,N′-trisubstituted guanidines from the addition reaction of anilines to carbodiimide, *Micro Nano Lett.*, 2020, **15**, 359–364, DOI: 10.1049/mnl.2019.0519.

29 S. A. Sarode, J. M. Bhojane and J. M. Nagarkar, An efficient magnetic copper ferrite nanoparticle catalysed ligand and solvent free synthesis of N-aryl amide from aldoximes and iodobenzene, *RSC Adv.*, 2015, **5**, 105353–105358, DOI: 10.1039/C5RA22777A.

30 T. P. Oliveira, S. F. Rodrigues, G. N. Marques, R. C. V. Costa, C. G. G. Lopes, C. Aranas, Jr., A. Rojas, J. H. G. Rangel and M. M. Oliveira, Synthesis, characterization, and photocatalytic investigation of $CuFe_2O_4$ for the degradation of dyes under visible light, *Catalysts*, 2022, **12**, 623, DOI: 10.3390/catal12060623.

31 R. Nisticò, R. Mantovan, M. Cantoni, C. Rinaldi, M. Malandrino, S. Mostoni, M. D'Arienzo, B. Di Credico and R. Scotti, Hydrothermal synthesis of Cu-substituted Ni ferrites: Structural, morphological, and magnetic properties, *J. Alloys Compd.*, 2024, **981**, 173628, DOI: 10.1016/j.jallcom.2024.173628.

32 V. P. Senthil, J. Gajendiran, S. G. Raj, T. Shanmugavel, G. R. Kumar and C. P. Reddy, Study of structural and magnetic properties of cobalt ferrite ($CoFe_2O_4$) nanostructures, *Chem. Phys. Lett.*, 2018, **695**, 19–23, DOI: 10.1016/j.cplett.2018.01.057.

33 J. Zhang, J. M. Song, H. L. Niu, C. J. Mao and S. Y. Zhang, $ZnFe_2O_4$ nanoparticles: Synthesis, characterization, and enhanced gas sensing property for acetone, *Sens. Actuators, B*, 2015, **221**, 55–62, DOI: 10.1016/j.snb.2015.06.040.

34 A. Kumar, N. Yadav, D. S. Rana, P. Kumar, M. Arora and R. P. Pant, Structural and magnetic studies of the nickel doped $CoFe_2O_4$ ferrite nanoparticles synthesized by the chemical co-precipitation method, *J. Magn. Magn. Mater.*, 2015, **394**, 379–384, DOI: 10.1016/j.jmmm.2015.06.087.

35 A. Boudjemaaa, I. Popescu, T. Juzsakovac, M. Kebir, N. Helailia, K. Bacharia and I. C. Marcu, M-substituted (M= Co, Ni and Cu) zinc ferrite photo-catalysts for hydrogen production by water photo-reduction, *Int. J. Hydrogen Energy*, 2016, **41**, 11108–11118, DOI: 10.1016/j.ijhydene.2016.04.088.

36 X. Shi, B. Chu, F. Wang, X. Wei, L. Teng, M. Fan, B. Li, L. Dong and L. Dong, Mn-modified CuO, $CuFe_2O_4$, and γ-Fe_2O_3 three-phase strong synergistic coexistence catalyst system for NO reduction by CO with a wider active window, *ACS Appl. Mater. Interfaces*, 2018, **10**, 40509–40522, DOI: 10.1021/acsami.8b13220.

37 T. M. Hammad, S. Kuhn, A. A. Amsha and R. Hempelmann, Investigation of structural, optical, and magnetic properties of Co^{2+} ions substituted $CuFe_2O_4$ spinel ferrite nanoparticles prepared via precipitation approach, *J. Australas. Ceram. Soc.*, 2021, **57**, 543–553, DOI: 10.1007/s41779-020-00556-z.

38 K. Verma, A. Kumar and D. Varshney, Effect of Zn and Mg doping on structural, dielectric and magnetic properties of tetragonal $CuFe_2O_4$, *Curr. Appl. Phys.*, 2013, **13**, 467–473, DOI: 10.1016/j.cap.2012.09.015.

39 T. Rodríguez-Flores, F. Shafiq and R. Nisticò, Synthesis, properties, and application in catalysis of Cu, Ni, Co, Zn ferrites: A comprehensive review study, *J. Alloys Compd.*, 2025, **1036**, 181926, DOI: 10.1016/j.jallcom.2025.181926.

40 T. M. Hammad, J. K. Salem, A. A. Amsha and N. K. Hejazy, Optical and magnetic characterizations of zinc substituted copper ferrite synthesized by a co-precipitation chemical method, *J. Alloys Compd.*, 2018, **741**, 123–130, DOI: 10.1016/j.jallcom.2018.01.123.

41 Z. Sun, L. Liu, D. Z. Jia and W. Pan, Simple synthesis of $CuFe_2O_4$ nanoparticles as gas-sensing materials, *Sens. Actuators, B*, 2007, **125**, 144–148, DOI: 10.1016/j.snb.2007.01.050.

42 T. H. Tran, M. H. Nguyen, T. H. T. Nguyen, V. P. T. Dao, P. M. Nguyen, V. T. Nguyen, N. H. Pham, V. V. Le, C. D. Sai, Q. H. Nguyen, T. T. Nguyen, K. H. Ho and Q. K. Doan, Effect of annealing temperature on morphology and structure of CuO nanowires grown by thermal oxidation method, *J. Cryst. Growth*, 2019, **505**, 33–37, DOI: 10.1016/j.jcrysgro.2018.10.010.

43 X. B. Zhong, Z. Z. Yang, H. Y. Wang, L. Lu, B. Jin, M. Zha and Q. C. Jiang, A novel approach to facilely synthesize mesoporous $ZnFe_2O_4$ nanorods for lithium-ion batteries, *J. Power Sources*, 2016, **306**, 718–723, DOI: 10.1016/j.jpowsour.2015.12.102.

44 J. Sun, Z. Wang, Y. Wang, Y. Zhu, T. Shen, L. Pang, K. Wei and F. Li, Synthesis of the nanocrystalline $CoFe_2O_4$ ferrite thin films by a novel sol–gel method using glucose as an additional agent, *Mater. Sci. Eng., B*, 2012, **177**, 269–273, DOI: 10.1016/j.mseb.2011.12.017.

45 A. C. Nawle, A. V. Humbe, M. K. Babrekar, S. S. Deshmukh and K. M. Jadhav, Deposition, characterization, magnetic and optical properties of Zn doped $CuFe_2O_4$ thin films, *J. Alloys Compd.*, 2015, **695**, 1573–1582, DOI: 10.1016/j.jallcom.2016.10.301.

46 M. A. Gabal, D. F. Katowah, M. A. Hussein, A. A. Al-Juaid, A. Awad, A. M. Abdel-Daiem, A. Saeed, M. M. Hessien and A. M. Asiri, Structural and magnetoelectrical properties of MFe_2O_4 (M = Co, Ni, Cu, Mg, and Zn) ferrospinels synthesized via an egg-white biotemplate, *ACS Omega*, 2021, **6**, 22180–22187, DOI: 10.1021/acsomega.1c02858.

47 M. Hashim, Alimuddin, S. Kumar, B. H. Koo, S. E. Shirsath, E. M. Mohammed, J. Shah, R. K. Kotnala, H. K. Choi, H. Chung and R. Kumar, Structural, electrical and magnetic properties of Co–Cu ferrite nanoparticles, *J. Alloys Compd.*, 2012, **518**, 11–18, DOI: 10.1016/j.jallcom.2011.12.017.

48 S. Park, S. Lee, H. Kim, J. Lee, J. Kim, J. Choi and Y. Kim, Rapid flame-annealed $CuFe_2O_4$ as efficient photocathode for solar-driven hydrogen production via photoelectrochemical water splitting, *ACS Sustainable Chem. Eng.*, 2019, **7**, 7047–7057, DOI: 10.1021/acssuschemeng.8b05824.

49 T. Lopes, L. Andrade, F. Le Formal, M. Grätzel, K. Sivula and A. Mendes, Hematite photoelectrodes for water splitting: evaluation of the role of film thickness by impedance spectroscopy, *Phys. Chem. Chem. Phys.*, 2014, **16**, 16515–16523, DOI: 10.1039/C3CP55473B.

50 M. Lao, Y. Zhang, Z. Liu, X. Zhang, Y. Zhang and X. Zhang, An in-depth understanding of alkaline hydrogen evolution reaction: From fundamentals and theories to heterostructured electrocatalyst design, *Nano Energy*, 2022, **98**, 107231, DOI: 10.1016/j.nanoen.2022.107231.

51 G. Lu, H. Yang, Y. Zhu, T. Huggins, Z. J. Ren, Z. Liu and W. Zhang, Synthesis of a conjugated porous Co(II) porphyrinylene–ethynylene framework through alkyne metathesis and its catalytic activity study, *J. Mater. Chem. A*, 2015, **3**, 4954–4959, DOI: 10.1039/C4TA06231K.

52 Y. Lin, Y. Wu, X. Jiang, Q. Wang, Y. Liu and L. Jin, Advancing bidirectional hydrogen spillover in heterostructure catalysts for electrocatalytic antimony removal and recovery from wastewater, *J. Hazard. Mater.*, 2026, **501**, 140662, DOI: 10.1016/j.jhazmat.2025.140662.

53 F. Lai, H. Shang, Y. Jiao, X. Chen, T. Zhang and X. Liu, Recent progress and perspective on electrocatalysis in neutral media: Mechanisms, materials, and advanced characterizations, *Interdiscip. Mater.*, 2024, **3**, 492–529, DOI: 10.1002/idm2.12172.

54 A. Raveendran, M. Chandran and R. Dhanusuraman, A comprehensive review on the electrochemical parameters and recent material development of electrochemical water splitting electrocatalysts, *RSC Adv.*, 2023, **13**, 3843–3876, DOI: 10.1039/d2ra07642j.

55 M. R. G. de Chialvo and A. J. Arvia, The electrochemical behaviour of copper in alkaline solutions containing sodium sulphide, *J. Appl. Electrochem.*, 1985, **15**, 685–696, DOI: 10.1007/BF00620564.

56 J. Durst, A. Siebel, C. Simon, F. Hasché, J. Herranz and H. A. Gasteiger, New insights into the electrochemical hydrogen oxidation and evolution reaction mechanism, *Energy Environ. Sci.*, 2014, **7**, 2255–2260, DOI: 10.1039/C4EE00440J.

57 D. Strmcnik, P. P. Lopes, B. Genorio, V. R. Stamenkovic and N. M. Markovic, Design principles for hydrogen evolution reaction catalyst materials, *Nano Energy*, 2016, **29**, 29–36, DOI: 10.1016/j.nanoen.2016.04.017.

58 N. Mahmood, Electrocatalysts for hydrogen evolution in alkaline electrolytes: Mechanisms, challenges, and prospective solutions, *Adv. Sci.*, 2018, **5**, 1700464, DOI: 10.1002/advs.201700464.

59 J. Zheng, A. Vojvodic and J. K. Nørskov, Universal dependence of hydrogen oxidation and evolution reactions on the hydrogen binding energy, *Sci. Adv.*, 2016, **2**, e1501602, DOI: 10.1126/sciadv.1501602.

60 S. Sudarsan, M. Anandkumar and E. A. Trofimov, Synthesis and characterization of copper ferrite nanocomposite from discarded printed circuit boards as an effective photocatalyst for Congo red dye degradation, *J. Ind. Eng. Chem.*, 2024, **131**, 208–220, DOI: 10.1016/j.jiec.2023.10.020.

61 H. Qin, Y. He, P. Xu, D. Huang, Z. Wang, H. Wang, Z. Wang, Y. Zhao, Q. Tian and C. Wang, Spinel ferrites (MFe2O4): Synthesis, improvement and catalytic application in environment and energy field, *Adv. Colloid Interface Sci.*, 2021, **294**, 102486, DOI: 10.1016/j.cis.2021.102486.

62 J. Zhang, X. Shang, H. Ren, J. Chi, H. Fui, B. Dong, C. Liu and Y. Chai, Modulation of inverse spinel Fe_3O_4 by phosphorus doping as an industrially promising electrocatalyst for hydrogen evolution, *Adv. Mater.*, 2019, **31**, 1905107, DOI: 10.1002/adma.201905107.

63 A. A. Rodríguez-Rodríguez, M. B. Moreno-Trejo, M. J. Meléndez-Zaragoza, V. Collins-Martínez, A. López-Ortiz, E. Martínez-Guerra and M. Sánchez-Domínguez, Spinel-type ferrite nanoparticles: Synthesis by the oil-in-water microemulsion reaction method and photocatalytic water-splitting evaluation, *Int. J. Hydrogen Energy*, 2019, **44**, 12421–12429, DOI: 10.1016/j.ijhydene.2018.09.183.

64 J. Prakash, R. Jasrotia, B. Lal, J. Ahmed, M. Fazil, S. Suman, A. Kandwal, V. Raja, T. Ahmad and S. K. Godara, Spinel cobalt nanostructures: Impact of calcination temperature on structural, microstructural, optical, magnetic, and photo/electrocatalytic traits towards HER, *Int. J. Hydrogen Energy*, 2025, **145**, 280–291, DOI: 10.1016/j.ijhydene.2025.05.432.

65 J. Prakash, R. Jasrotia, S. Suman, J. Ahmed, S. M. Alshehri, T. Ahmad, M. Fazil, M. Sillanpää, N. Lakshmaiya and V. Raja, Nickel substituted cobalt nanoferrites for advanced photocatalytic and electrocatalytic green hydrogen generation, *J. Mol. Struct.*, 2024, **1321**, 140162, DOI: 10.1016/j.molstruc.2024.140162.

66 K. R. Sánchez-Lievanos, M. Tariq, W. W. Brennessel and K. E. Knowles, Mesoporous nickel ferrites with spinel structure prepared by a sol–gel method, *Sol. Energy Mater. Sol. Cells*, 2020, **206**, 110786, DOI: 10.1016/j.solmat.2020.110786.

67 A. Sharma, A comprehensive review on the spinel nanomaterials for photocatalytic and electrocatalytic applications, *J. Mol. Struct.*, 2025, **1348**, 143348, DOI: 10.1016/j.molstruc.2025.143348.

68 R. Jasrotia, C. K. Chan, M. Fazil, J. Ahmed, T. Ahmad, N. Alhokbany, M. Sillanpää, N. Lakshmaiya and V. Raja, High performance Sm substituted Ni–Zn catalysts for green hydrogen generation via photo/electro catalytic water splitting processes, *J. King Saud Univ., Sci.*, 2024, **36**, 103426, DOI: 10.1016/j.jksus.2024.103426.

69 Q. Yang, J. Du, X. Nie, D. Yang, L. Bian, L. Yang, F. Dong, H. He, Y. Zhou and H. Yang, Magnetic field-assisted photoelectrochemical water splitting: The photoelectrodes have weaker nonradiative recombination of carrier, *ACS Catal.*, 2021, **11**, 1242–1247, DOI: 10.1021/acscatal.0c05436.

70 H. Pan, X. Jiang, X. Wang, Q. Wang, M. Wang and Y. Shen, Effective magnetic field regulation of the radical pair spin states in electrocatalytic CO_2 reduction, *J. Phys. Chem. Lett.*, 2020, **11**, 48–53, DOI: 10.1021/acs.jpclett.9b03146.

71 C. Niether, S. Faure, A. Bordet, J. Deseure, M. Chatenet, J. Carrey, B. Chaudret and A. Rouet, Improved water electrolysis using magnetic heating of FeC–Ni core–shell nanoparticles, *Nat. Energy*, 2018, **3**, 476–483, DOI: 10.1038/s41560-018-0132-1.